

## Chapter 2

# Principle Component Analysis and Linear Optics

## 2.1 Introduction

Principle component analysis (PCA) is a widely used technique in multivariate statistics to identify dominant patterns in a given dataset. This is accomplished by a transformation to pick a coordinate axis that maximizes the variance of all data points along that axis [24, 25, 26]. For a given dataset  $X$ , the unit length basis vectors  $\mathbf{v} = [v_1, v_2, \dots, v_n] \in \mathcal{R}^M$  that maximize the variance is evaluated as

$$\frac{\mathbf{v}^T C_{ij} \mathbf{v}}{\mathbf{v}^T \mathbf{v}} = \max \quad (2.1)$$

where

$$C_{ij} = \frac{1}{n-1} \sum_{i,j=0}^n (X_i - \bar{X})(X_j - \bar{X}) \quad (2.2)$$

is the covariance matrix ( $\text{cov}\{X_i, X_j\}$ ). Subsequent orthogonal axes can be computed to form a set of basis vectors that completely define the dataset with a reduced dimensionality. Using this transformation, the original data matrix  $X_{n \times m}$  can be decomposed as

$$X = WV^T \quad (2.3)$$

where  $W_{n \times m}$  and  $V_{m \times m}$  comprise of orthogonal vectors describing the spatial<sup>1</sup> and temporal<sup>2</sup> behavior of the leading principle components. This decomposition is mathematically equivalent to a singular value decomposition (SVD).

---

<sup>1</sup>Behavior of the principle components at the each monitor position.

<sup>2</sup>Time evolution of a principle component.

## 2.2 Singular Value Decomposition

Any  $n \times m$  real or complex matrix  $X$  can be factorized into the form

$$X = U\Sigma V^\dagger \quad (2.4)$$

where  $U$  is an  $n \times n$  unitary matrix,  $\Sigma$  is a  $n \times m$  diagonal matrix, and  $V^\dagger$  is the Hermitian conjugate of an  $m \times m$  unitary matrix [27]. Both  $U$  and  $V$  are hermitian, such that

$$XX^\dagger = U\Sigma^2U^\dagger, \quad X^\dagger X = V\Sigma^2V^\dagger \quad (2.5)$$

The diagonal elements of  $\Sigma$  represent the square roots of the eigenvalues of covariance matrix  $X^\dagger X$  or  $XX^\dagger$  and are referred to as singular values. The number of non-zero singular values reveals the dimensionality of the data set. Since  $U$  and  $V$  are unitary matrices, the vectors of  $\{u_1, u_2, \dots, u_n\}$  and  $\{v_1, v_2, \dots, v_m\}$  form an orthonormal basis of  $X$ .

SVD has found many applications, especially in data processing and numerical problems. The most direct application of SVD is the computation of eigenvalues of  $cov\{X_i, X_j\}$ . Unlike the computation of eigenvalues using traditional algorithms, SVD is robust against perturbations and roundoff errors [28]. A perturbation in the data matrix can be decomposed as

$$A + \delta A = U(\Sigma + \delta\Sigma)V^\dagger \quad (2.6)$$

Since  $U$  and  $V$  are unitary, they have a unit norm, and  $||\delta A|| = ||\delta\Sigma||$ . Therefore, perturbations in the data matrix manifest themselves as perturbations in singular values of the same order. Given a rectangular matrix, the SVD essentially computes a pseudo-inverse which naturally lends itself to least square problems extensively used in physics. The rank of the matrix is easily estimated from the number of non-zero singular values which determines the minimum number of modes to completely describe the system. Since the factorization groups the data into basis vectors, the reduced dimensionality is very useful for data and image compression schemes.

The distribution of multiple BPMs along the beam trajectory and their capability to acquire several sequential TBT data is ideal for multivariate time series analysis to understand the underlying structure of the lattice. Since the BPM data is a collection of space-time series, SVD factorizes the information into

$$B(\mathbf{x}, t) = \sum_n \sigma_n U_n(t) V_n(\mathbf{x}) \quad (2.7)$$

where,  $U_n$  and  $V_n$  are the eigenmodes of the “spatial” and “temporal” correlation matrices

$$C(x_i, x_j) = \sum_t B(x_i, t)B(x_j, t) \quad (2.8)$$

$$C(t_i, t_j) = \sum_x B(x, t_i)B(x, t_j) \quad (2.9)$$

In this chapter we focus on the application of SVD on TBT data from the BPMs to infer beam phase space and corresponding lattice parameters. This numerical technique was first applied to beam physics by J. Irwin and group [29]. A detailed treatment of transverse beam dynamics in 1D (no transverse coupling) using PCA-SVD formalism can be found in Refs. [30, 31]. Independent component analysis, another numerical approach (similar to PCA) using a blind source separation technique has also been applied to study BPM signals of interest [32]. We outline the application of SVD on BPM data and present measurements of RHIC optics using this formalism and betatron oscillations excited by ac dipoles.

## 2.3 Linear Optics: Formalism

Assuming, the motion is dominated by betatron motion without coupling, the data from  $m$  BPMs recording  $t$  turns each can be represented in a matrix form. This BPM matrix can be factorized as

$$\underbrace{\begin{pmatrix} b_1^1 & b_1^2 & \dots \\ b_2^1 & \ddots & \\ b_3^1 & & \\ \vdots & & \end{pmatrix}}_{B_{t \times m}} = \underbrace{\begin{pmatrix} u_1^+ & u_1^- & \dots \\ \vdots & \vdots & \\ \vdots & \vdots & \\ u_t^+ & u_t^- & \dots \end{pmatrix}}_{U_{t \times m}} \underbrace{\begin{bmatrix} \sigma_+ & 0 & \dots & \dots \\ 0 & \sigma_- & & \\ \vdots & & \ddots & \\ \vdots & & & \sigma_m \end{bmatrix}}_{\Sigma_{m \times m}} \underbrace{\begin{bmatrix} v_1^+ & v_1^- & \dots \\ \vdots & \vdots & \\ \vdots & \vdots & \\ v_m^+ & v_m^- & \dots \end{bmatrix}^T}_{V_{m \times m}^T} \quad (2.10)$$

where “+” and “-” represent the orthogonal vectors representing a betatron mode.  $\Sigma_{m \times m} = [\sigma^+, \sigma^-, \dots]$ ,  $V_{m \times m} = [v^+, v^-, \dots]$ , and  $U_{t \times m} = [u^+, u^-, \dots]$ , are the corresponding non-negative singular values, eigenvectors representing the spatial variation of betatron function, and temporal eigenvectors representing the time evolution of the betatron mode respectively.

The TBT data in the  $m^{th}$  BPM can be expressed as

$$b_t^m = \sqrt{2J_t\beta_m} \cos(\phi_t + \psi_m) \quad (2.11)$$

The BPM matrix is normalized by the number of turns  $B = b_t^m / \sqrt{T}$ , therefore the covariance matrix is given by

$$C_B^{mn} = \frac{1}{T} \sum_{t=1}^T b_t^m b_t^n \quad (2.12)$$

$$= \sum_{t=1}^T \frac{J}{T} \sqrt{\beta_m \beta_n} [\cos(\psi_m - \psi_n) + \cos(2\phi_t + \psi_m + \psi_n)] \quad (2.13)$$

$$= \langle J \rangle \sqrt{\beta_m \beta_n} \cos(\psi_m - \psi_n) \quad (2.14)$$

To find the eigenvalues and eigenvectors, we need to solve

$$C_B v = \lambda v \quad (2.15)$$

where  $v = \sqrt{2J\beta_m} \cos(\phi_0 + \psi_m)$ . From the  $m^{\text{th}}$  component of the secular equation we have the condition that

$$\sum_{n=1}^M \beta_n \sin 2(\phi_0 + \psi_n) = 0. \quad (2.16)$$

The two solutions for Eq. 2.16 are

$$\phi_0 = -\frac{1}{2} \tan^{-1} \left( \frac{\sum_n \beta_n \sin 2\psi_n}{\sum_n \beta_n \cos 2\psi_n} \right) \quad (2.17)$$

and  $\phi_0 + \pi/2$  corresponding to the two eigenvalues

$$\lambda_{\pm} = \frac{1}{2} \langle J \rangle \left[ \sum_{n=1}^M \beta_n \pm \sum_{n=1}^M \beta_n \cos 2(\phi_0 + \psi_n) \right]. \quad (2.18)$$

The normalized eigenvectors (spatial) are given by

$$v_+ = \frac{1}{\sqrt{\lambda_+}} \left[ \sqrt{\langle J \rangle \beta_m} \cos(\phi_0 + \psi_m) \right] \quad (2.19)$$

$$v_- = \frac{1}{\sqrt{\lambda_-}} \left[ \sqrt{\langle J \rangle \beta_m} \sin(\phi_0 + \psi_m) \right] \quad (2.20)$$

and the corresponding, normalized temporal vectors are given by

$$u_+ = \sqrt{\frac{2J_t}{T\langle J \rangle}} \cos(\phi_t - \phi_0) \quad (2.21)$$

$$u_- = -\sqrt{\frac{2J_t}{T\langle J \rangle}} \sin(\phi_t - \phi_0) \quad (2.22)$$

Therefore, the Twiss functions <sup>3</sup> can be derived from the betatron vectors

$$\psi = \tan^{-1} \left( \frac{\sigma_- v_-}{\sigma_+ v_+} \right) \quad (2.23)$$

$$\beta = \langle J \rangle^{-1} (\sigma_+^2 v_+^2 + \sigma_-^2 v_-^2) \quad (2.24)$$

Error bounds in the Twiss functions are

$$\sigma_\psi = \sqrt{\left( \frac{\partial \psi}{\partial \sigma_+} \right)^2 \sigma_+^2 + \left( \frac{\partial \psi}{\partial \sigma_-} \right)^2 \sigma_-^2} \approx \frac{1}{\sqrt{T}} \frac{\sigma_r}{\sigma_s} \sqrt{\frac{\langle \beta \rangle}{2\beta}} \quad (2.25)$$

$$\sigma_{\frac{\Delta\beta}{\beta}} = \sqrt{\left( \frac{\partial \beta}{\partial \sigma_+} \right)^2 \sigma_+^2 + \left( \frac{\partial \beta}{\partial \sigma_-} \right)^2 \sigma_-^2} \approx 2\beta\sigma_\psi \quad (2.26)$$

## 2.4 RHIC Linear Optics: Measurements

The RHIC lattice consists of 6 arcs, each with 11 FODO<sup>4</sup> cells with approximately 80° phase advance. Parameters of the arc dipoles and quadrupoles are shown in Table 1.2. Each of the six interaction region (IRs) consists of a triplet quadrupole scheme to focus the beams at the collision point, and a pair of *D0* and *DX* dipole magnets to bring the beams in and out of collision. A schematic of the final focus IR (6 o'clock) is shown Fig. 2.1. A section between the final focus and arc consists of FODO cells similar to the arc with a few dipoles for dispersion suppression. The “ideal”  $\beta$  functions and dispersion functions near an IR are plotted a function of longitudinal position in Fig. 2.2. Optics in Fig. 2.1 are for proton-proton collisions with  $\beta^* = 1m$  at the collision point.

Limitations in measuring Twiss functions are primarily related to the quality and availability of reliable BPM data. At RHIC, a significant number of BPMs exhibit failures related to radiation, electronics and low level software issues which are discussed in chapter 3 and Ref. [19]. These BPMs are excluded from the calculation of Twiss parameters. It was also found that a few BPMs show turn mismatch due to timing problems in the electronics which is corrected for 1-2 turns mismatch because the phase advance between two consecutive BPMs are usually smaller than  $\pi/2$ . Beyond three turns, this correction can lead to ambiguous results and the only remedy is to fix the timing

<sup>3</sup>The parameters  $\beta$ ,  $\alpha$ , and  $\gamma$  are also called Twiss functions [8]

<sup>4</sup>A pair of focusing and defocusing quadrupoles inter-spaced by a bending dipole magnet or a drift space

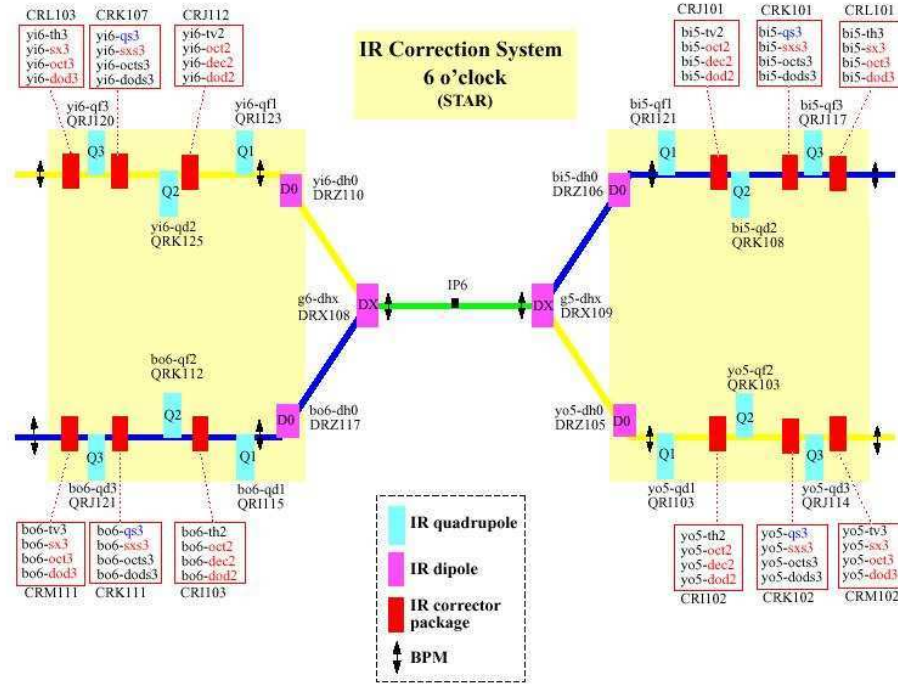


Figure 2.1: The 6 o'clock IR final-focus region with triplet quadrupoles,  $D0$  and  $DX$  bending dipoles, and linear and non-linear correctors (courtesy F. Pilat).

at the hardware level using simulated beam signals or with a circulating beam with a single injected bunch.

Optics measurements were taken at injection during a working point scan during Run 2004 [20]. Figs. 2.3 and 2.4 show a comparison between model and measured Twiss functions for Au-Au injection ( $\gamma = 10.25$ ) and p-p injection ( $\gamma = 25.94$ ). The rms of the phase advance difference,  $(\psi_m^{model} - \psi_m^{measured})$  and the rms of relative difference in  $\beta$  function,  $(\beta_m^{model} - \beta_m^{meas})/\beta_m^{model}$  were calculated to understand the sensitivity of optics measurements to the working point and  $\beta^*$ . Some measurements show a large deviation from the model mainly due to BPM failures. Data files with very large deviation are not included in this analysis. The measurements for Yellow and Blue ring were not separated because we assume that the instrumentation in both rings were similar.

Tables 2.1 and 2.2 show a detailed list of rms differences for the different working points at injection and store. Note that the model tunes are not exactly matched to measured tunes [21]. Fig. 2.5 shows a plot of average

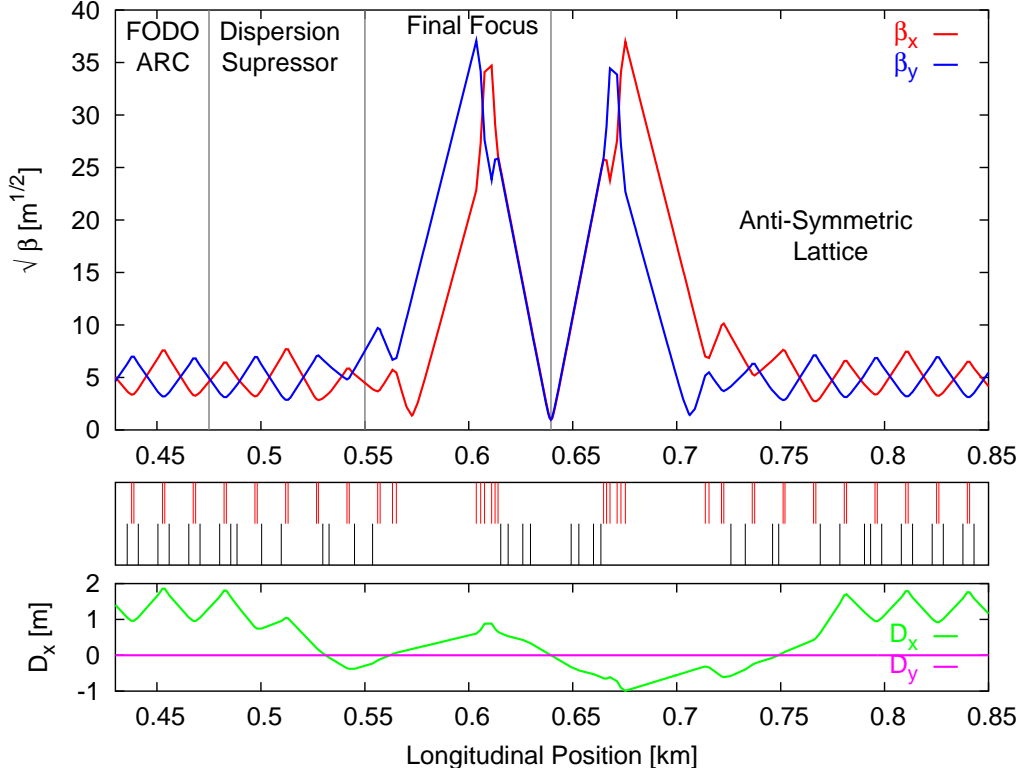


Figure 2.2:  $\beta$  functions (top) and dispersion functions (bottom) at the 6 o'clock IR region. A representation of the lattice (dipoles in black and quadrupoles in red) is shown in the middle. The betatron tunes are  $Q_x = 28.23$  and  $Q_y = 28.22$ , and the horizontal dispersion at the collision point is zero.

values and their standard deviations of  $(\Delta\beta/\beta)^{rms}$  and  $\Delta\psi^{rms}$  only for Au-Au and p-p injection and store conditions. The other working points are not plotted because of large systematic errors. It is clear from Fig. 2.5 that large deviation from the mean values are mainly due to systematic errors. A number of systematic measurements and improvements in BPM reliability will reduce these deviations significantly. One can notice that the rms phase advance difference for  $Q \sim 0.2$  region appears to be slightly better than  $Q \sim 0.7$  region. One can also notice that for  $Q \sim 0.2$  region, the  $(\Delta\beta/\beta)^{rms}$  is smaller for injection optics ( $\beta^* = 10\text{m}$ ) than store optics ( $\beta^* = 1\text{m}$ ) as expected. However, the region near  $Q \sim 0.7$  shows contrary results which needs to be verified. A large number of statistics are needed to arrive at a definitive conclusion.

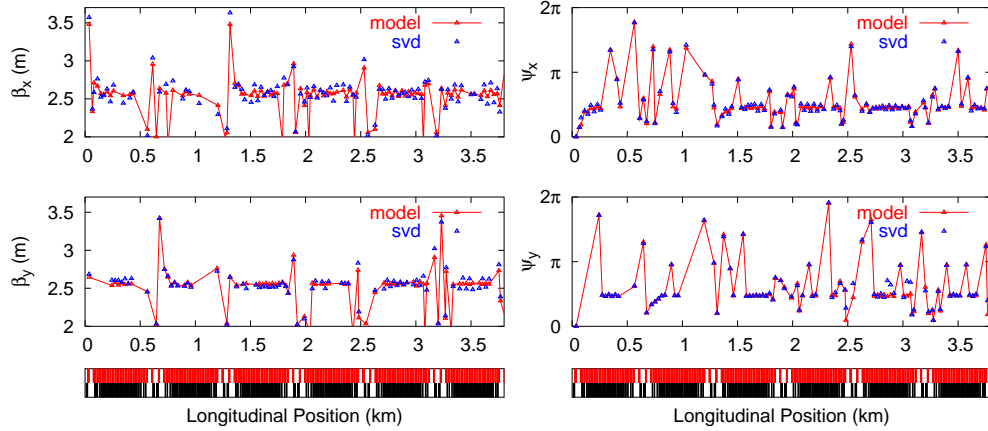


Figure 2.3: Phase advance and beta function for Au-Au injection optics using AC dipoles.

## 2.5 Error source identification

Closed orbit correction due to random dipole errors has been extensively studied [33, 34]. Global techniques using linear least square algorithms and local orbit bumps are routinely used in most accelerators to correct the particle orbit. A thin horizontal focusing error of  $\Delta q$  [ $\text{m}^{-1}$ ] causes a horizontal perturbation wave that propagates ( $\beta$ -beat) downstream to first order in  $\Delta q$  like

$$\frac{\Delta\beta}{\beta} \approx -\Delta q \beta_0 \sin(2(\phi - \phi_0)) \quad (2.27)$$

where  $\beta_0$  is the design horizontal beta function at the quadrupole error source. The close analogy between particle trajectory and beta wave perturbation indicates a close connection between the problems of closed orbit correction and quadrupole error source identification.

### 2.5.1 Global Correction

The effect of the  $\beta$  function perturbation at  $m$  BPMs due to change in strength of  $n$  correctors can be formulated into a  $m \times n$  response matrix (similar to closed orbit response matrix)

$$\mathcal{A}\Delta\vec{q} = \left[ \frac{\Delta\vec{\beta}}{\vec{\beta}} \right] \quad (2.28)$$



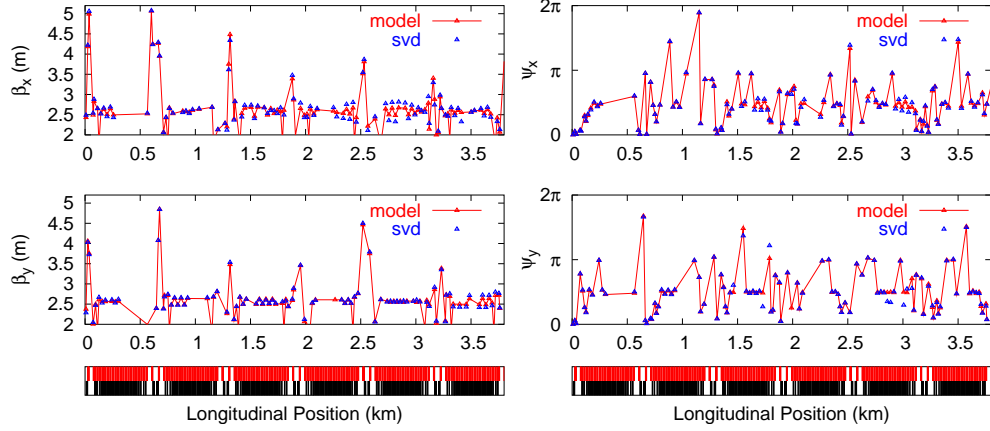


Figure 2.4: Phase advance and beta function for p-p injection optics using AC dipoles.

where

$$\mathcal{A}_{mn} = \frac{\beta_n}{2 \sin(2\pi Q)} \cos(2|\psi_m - \psi_n| - 2\pi Q). \quad (2.29)$$

The model and measured  $\beta$ -functions at  $m$  BPMs can be expressed into a  $\beta$ -beat vector

$$\left[ \frac{\Delta \vec{\beta}}{\vec{\beta}} \right] = \left[ \left( \frac{\Delta \beta}{\beta} \right)_1, \left( \frac{\Delta \beta}{\beta} \right)_2, \dots, \left( \frac{\Delta \beta}{\beta} \right)_m \right] \quad (2.30)$$

The goal is to minimize the quadratic residual  $\beta$ -beat at all the BPMs

$$\left\| \mathcal{A} \Delta \vec{q} - \frac{\Delta \vec{\beta}}{\vec{\beta}} \right\|^2 = \min. \quad (2.31)$$

For  $m = n$ , the solution for this linear equation is unique and is given by

$$\Delta \vec{q} = (\mathcal{A}^T \mathcal{A})^{-1} \mathcal{A}^T \left[ \frac{\Delta \vec{\beta}}{\vec{\beta}} \right] \quad (2.32)$$

and for

$$\begin{array}{ll} m > n & : \text{ over-determined } \quad \{ \text{minimum residual} \} \\ m < n & : \text{ over-constrained } \quad \{ \|\Delta \vec{q}\| \rightarrow \min \} \end{array} \quad (2.33)$$

which can be easily solved using numerical techniques like SVD.

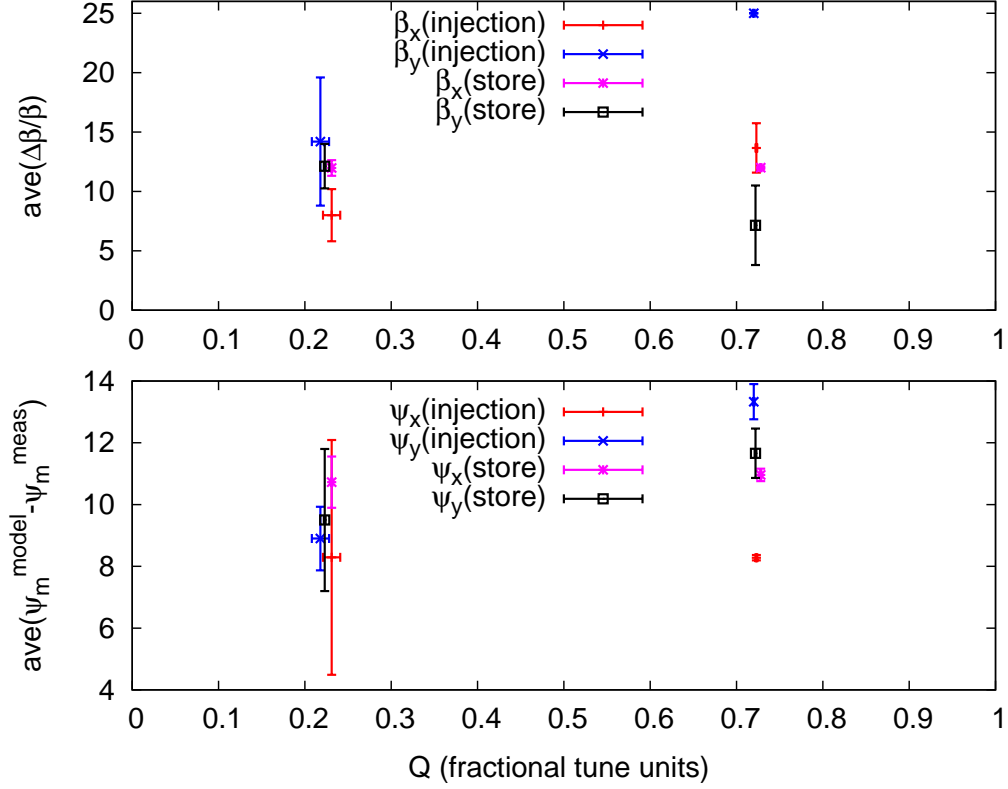


Figure 2.5: RMS relative differences of phase and  $\beta$  functions between model and measured values. The data points represent the different working points for Au-Au and p-p beams at both injection and store.

### 2.5.2 Local Correction

Just as 3 dipole correctors can be powered to create a closed orbit “three-bump”, so also can 3 quadrupoles create a local  $\beta$ -bump. The local  $\beta$  perturbation by three quadrupoles require

$$\beta_1 \Delta q_1 C(\psi_{31} - 2\pi Q) + \beta_2 \Delta q_2 C(\psi_{32} - 2\pi Q) + \beta_3 \Delta q_3 C(2\pi Q) = 0 \quad (2.34)$$

$$\beta_1 \Delta q_1 C(2\pi Q) + \beta_2 \Delta q_2 C(\psi_{21} - 2\pi Q) + \beta_3 \Delta q_3 C(\psi_{13} - 2\pi Q) = 0 \quad (2.35)$$

where “ $C$ ” is the cosine function. Therefore, the strengths of the three quadrupoles to make a closed  $\beta$ -bump are

$$\begin{aligned}\Delta q_1 &= -\frac{\Delta\beta_2}{\beta_2} \frac{1}{\beta_1} \frac{1}{\sin(2\psi_{21})} \\ \Delta q_2 &= +\frac{\Delta\beta_2}{\beta_2} \frac{1}{\beta_2} \frac{\sin(2\psi_{31})}{\sin(2\psi_{32}) \sin(2\psi_{21})} \\ \Delta q_3 &= -\frac{\Delta\beta_2}{\beta_2} \frac{1}{\beta_3} \frac{1}{\sin(2\psi_{32})}\end{aligned}\tag{2.36}$$

and where, for example,

$$\psi_{21} = \psi_2 - \psi_1\tag{2.37}$$

It should be noted that the  $\beta$ -bump is not closed in the other (vertical) plane. The “sliding 3-bump” algorithm can take the measured  $\Delta\beta/\beta$  at many BPMs vector as input, generating a suggested quadrupole correction vector (with elements at every lattice quadrupole) as output. It is often more practical to interpret this output vector as a set of quadrupole error sources, especially if the quadrupoles are powered in families (as in RHIC). If independent horizontal and vertical optics error measurements are available, then both measurements should identify the same quadrupole error sources. An off-line code  **$\beta$ -beat** is developed to automate source identification. Simulations to predict quadrupole errors in LHC and correct  $\beta$ -beat below the 20% level<sup>5</sup> in this fashion is under study [35].

## 2.6 Summary

An outline of PCA, SVD and their applications to linear optics in colliders is discussed. The measurement of linear optics using AC dipole data was demonstrated reliably in Run 2003-04. Optics were measured for different working point tunes and a comparison for each working point was done to understand the effect of tune. Although the region near  $Q \sim 0.2$  shows slightly better results than the region near  $Q \sim 0.7$ , no significant difference was found between the working points. The effect of  $\beta^*$  on the magnitude of  $\beta$ -beat is consistent for data near  $Q \sim 0.2$  region. The region near  $Q \sim 0.7$  needs to be revisited and more systematic studies will help develop a more accurate model. For all measurements faulty BPMs were removed based on criteria explained in the chapter 3.

---

<sup>5</sup>LHC aperture constraint for maximum allowable  $\beta$ -beat.

Table 2.1: Working point optics at Injection( $\gamma_{Au} - 10.52$ ,  $\gamma_{pp} - 25.94$ ).  $\beta^*$  @ 6 IPs (10,10,10,10,10,10) [m]. NE - Not Estimated due to excitation of AC dipole in only one plane or large systematic errors.

Ring	$Q_x$	$Q_y$	$\Delta\psi_x^{rms}$	$\frac{\Delta\beta_x^{rms}}{\beta_x}$	$\Delta\psi_y^{rms}$	$\frac{\Delta\beta_y^{rms}}{\beta_x}$
RHIC Tunes: Au-Au						
B	0.237	0.222	11.9	8 %	NE	NE
B	0.237	0.222	11.31	7 %	9.4	12 %
Y	0.21	0.22	10.9	NE	10.4	14 %
B	0.238	0.20	6.7	10 %	8.27	8 %
B	0.238	0.20	5.9	11 %	8.6	18 %
Y	0.219	0.232	2.5	5 %	8.6	17 %
B	0.238	0.224	11.46	7 %	10.1	23 %
B	0.238	0.224	NE	NE	7.5	8 %
RHIC Tunes: p-p						
Y	0.723	0.720	8.19	12 %	14	25 %
Y	0.723	0.720	8.3	13 %	13	NE
Y	0.723	0.720	8.36	16 %	13	NE
RHIC Design Tunes: Au-Au						
Y	0.168	0.182	16.1	48 %	9.57	NE
Y	0.168	0.182	4.79	33 %	NE	NE
Y	0.201	0.187	2.13	19 %	9.8	32 %
Y	0.201	0.187	15.4	39 %	6.5	12 %
ISR Tunes (Au-Au)						
B	0.1025	0.11	10.9	13 %	22.3	52 %
B	0.1025	0.11	NE	NE	22.4	31 %
B	0.1025	0.11	NE	NE	15	8 %
SPS Tunes (Au-Au)						
B	0.705	0.695	13.3	25 %	20.07	39 %
B	0.705	0.695	17.0	23 %	17.7	36 %
B	0.705	0.695	NE	NE	14.5	9 %
B	0.705	0.695	NE	NE	12.3	9 %

Table 2.2: Working Point Optics at Store with ( $\gamma_{Au} = 10.52$ ,  $\gamma_{pp} = 106.58$ ).

Ring	$Q_x$	$Q_y$	$\Delta\psi_x^{rms}$	$\frac{\Delta\beta_x^{rms}}{\beta_x}$	$\Delta\psi_y^{rms}$	$\frac{\Delta\beta_y^{rms}}{\beta_x}$
RHIC Tunes Au-Au $\beta^*(3,5,1,1,3,5)$ [m], $\gamma = 107.76$						
B	0.231	0.223	10.3	12 %	8.0	11 %
B	0.231	0.223	10.7	13 %	7.0	11 %
B	0.231	0.223	10.0	13 %	11.2	12 %
B	0.231	0.223	11.9	12 %	11.9	15 %
RHIC Tunes p-p $\beta^*(3,10,2,2,3,10)$ [m], $\gamma = 106.58$						
Y	0.728	0.722	10.8	12 %	10.7	11 %
Y	0.728	0.722	10.9	12 %	11.93	6 %
Y	0.728	0.722	11.19	12 %	12.36	5 %